RESTORATION OF ULTRASOUND IMAGES USING SPATIALLY-VARIANT KERNEL DECONVOLUTION

Mihai I. Florea[⋆] *Adrian Basarab*[†] *Denis Kouamé*[†] *Sergiy A. Vorobyov*[⋆]

[⋆] Department of Signal Processing and Acoustics, Aalto University, Espoo, Finland
[†]IRIT UMR CNRS 5505, University of Toulouse, Toulouse, France

ABSTRACT

Most of the existing ultrasound image restoration methods consider a spatially-invariant point-spread function (PSF) model and circulant boundary conditions. While computationally efficient, this model is not realistic and severely limits the quality of reconstructed images. In this work, we address ultrasound image restoration under the hypothesis of piece-wise linear vertical variation of the PSF based on a small number of prototypes. No assumption is made on the structure of the prototype PSFs. To regularize the solution, we use the classical elastic net constraint. Existing methodologies are rendered impractical either due to their reliance on matrix inversion or due to their inability to exploit the strong convexity of the objective. Therefore, we propose an optimization algorithm based on the Accelerated Composite Gradient Method, adapted and optimized for this task. Our method is guaranteed to converge at a linear rate and is able to adaptively estimate unknown problem parameters. We support our theoretical results with simulation examples.

Index Terms— Accelerated Composite Gradient Method, point-spread function, reconstruction, restoration, spatially varying, ultrasound

1. INTRODUCTION

Ultrasound imaging is an efficient, cost effective, and safe medical imaging modality. It is widely used for various clinical applications and is especially well suited for the diagnosis of soft tissue pathologies. These advantages are however mitigated by the relative low image quality, in terms of signal-to-noise ratio, low contrast, and poor spatial resolution. The main factors affecting the quality of ultrasound images are the finite bandwidth and aperture of the imaging transducer as well as the physical phenomena (e.g., diffraction and attenuation) related to the propagation of sound waves in human tissues. Consequently, a rich body of scientific literature addresses ultrasound image reconstruction, i.e., the estimation of the tissue reflectivity function (TRF) from ultrasound images. Generally, existing approaches turn the TRF estimation into a deconvolution problem, by considering, under the first order Born approximation, that the formation of ultrasound images follows a 2D convolution model between the TRF and the system point-spread function (PSF). The PSF can be either estimated in a pre-processing step (see, e.g., [1–6]) or jointly estimated with the TRF, *i.e.*, blind deconvolution (see, e.g., [7–10]). Mainly for computational reasons, most of the existing ultrasound image restoration methods consider a spatially-invariant PSF model and circulant boundary conditions. However, independently of the acquisition setup, stationary convolution cannot accurately model the formation of ultrasound images. To overcome this issue, ultrasound images are generally divided in local regions prior to deconvolution, assuming a block-wise spatially-invariant PSF (see, e.g., [11]). To avoid issues related to stitching together the results of block-wise techniques, a few attempts have been very recently made in [12] and [13] to account for non-stationary convolution models in ultrasound imaging. The former relies on a very restrictive model with few degrees of freedom whereas the deconvolution method in the latter is computationally intractable for large images.

This paper proposes an optimization algorithm adapted to ultrasound image restoration under the hypothesis of spatially-variant PSF. The convolution kernel is assumed to be horizontally invariant but to vary vertically as a linear combination of neighboring prototype point-spread functions (PSF). To regularize the solution of the inverse problem generated by this model, we use herein the classical elastic net constraint [14]. Elastic net ensures a compromise between the ℓ_1-norm promoting sparse solutions and the ℓ_2-norm imposing smooth results. Its interest in ultrasound imaging has been already shown through different applications, e.g. compressed sensing [15], beamforming [16] or clutter filtering [17]. The elastic net regularized inverse problem has a non-differentiable objective and a large number of optimization variables. Therefore, it can only be addressed using proximal gradient schemes. The proposed method, based on the Accelerated Composite Gradient Method (ACGM) [18, 19], is able to simultaneously exploit the strong convexity of the problem and automatically provide a tight local estimate of the otherwise unknown Lipschitz constant.

2. PROBLEM FORMULATION

The acquisition model considered in this work is given by

$$\boldsymbol{y} = \boldsymbol{H}\boldsymbol{P}\boldsymbol{x} + \boldsymbol{n}, \tag{1}$$

where $\boldsymbol{y}$ denotes the observed image, $\boldsymbol{x}$ is the tissue reflectivity function (TRF) to be recovered and $\boldsymbol{n}$ represents independent identically distributed additive white Gaussian noise. All images are of the same size, $\boldsymbol{x}, \boldsymbol{y}, \boldsymbol{n} \in \mathcal{D}_f \stackrel{\text{def}}{=} \mathbb{R}^{m_t \times n_t}$, where m_t denotes the height (number of pixels along the axial dimension) and n_t gives the width (lateral pixel count) of the TRF. The linear operator $\boldsymbol{P}$ pads the TRF with a $m_r \times n_r$ boundary, yielding an image of size $m_p \times n_p$, where $m_p = m_t + 2m_r$ and $n_p = n_t + 2n_r$, respectively. Our model accounts for any simple form of padding[1].

The linear operator $\boldsymbol{H}$ performs the spatially-variant kernel convolution. Within a classical pulse-echo acquisition scheme, focused

Part of this work has been supported by the Academy of Finland, under grant no. 299243, and CIMI Labex, Toulouse, France, under grant ANR-11-LABX-0040-CIMI within the program ANR-11-IDEX-0002-02.

[1]See [20] for a detailed discussion on simple padding and its implementation.

ultrasound waves are sequentially emitted by a sliding active subaperture. For each emission, the raw data is collected by the elements within the active aperture and further beamformed to compute an A-line representing one column of the ultrasound image. For this reason, the PSF can be reasonably considered spatially-invariant in the lateral (horizontal) direction. However, despite dynamic focusing in reception and time gain compensation, the PSF strongly varies in the axial (vertical) direction, *i.e.*, in the direction of ultrasound wave propagation, degrading spatial resolution away from the focal depth.

In our model, we account for this axial variation by assuming that a small number n_k of prototype kernels is known, each prototype PSF $\boldsymbol{K}_q$ having a center at row c_q for all $q \in \{1, ..., n_k\}$. The prototype PSFs are sorted by c_q and thus the values of c_q form a partition of the set of rows. The kernels of each row are computed using linear interpolation. Specifically, kernels above c_1 are equal to $\boldsymbol{K}_1$, those below c_{n_k} equal $\boldsymbol{K}_{n_k}$. The kernels of all other rows are obtained as a convex combination (alpha-blending) of the prototype PSF above and the one below that row, the proportion given by the relative distance to the two centers.

Every row produced by the linear operator $\boldsymbol{H}$ is obtained by taking the corresponding row in the input image (padded TRF) along with all pixels within a boundary of size $m_p \times n_p$ and performing discrete valid convolution with the kernel pertaining to that row, obtained as explained above. It follows that the padding boundary size has to match the prototype PSF radii. The use of discrete valid convolution is the reason behind the need for padding the TRF with $\boldsymbol{P}$.

Our acquisition model can be used to construct a deconvolution problem which seeks to minimize the additive white Gaussian noise subject to regularization. When employing the elastic net, the TRF can be obtained by solving the following optimization problem

$$\min_{\boldsymbol{x} \in \mathcal{D}_f} \frac{1}{2}\|\boldsymbol{HPx} - \boldsymbol{y}\|_2^2 + \lambda_1\|\boldsymbol{x}\|_1 + \frac{\lambda_2}{2}\|\boldsymbol{x}\|_2^2. \tag{2}$$

3. PROPOSED METHOD

To efficiently solve optimization problem (2) for any non-negative value of λ_2, we propose a variant of the Accelerated Composite Gradient Method (ACGM) [18, 19] optimized for the elastic net[2].

The objective F in problem (2) can be split into a quadratic function f and an elastic net regularizer Ψ as follows:

$$f(\boldsymbol{x}) = \frac{1}{2}\|\boldsymbol{Ax} - \boldsymbol{y}\|_2^2, \quad \Psi(\boldsymbol{x}) = \lambda_1\|\boldsymbol{x}\|_1 + \frac{\lambda_2}{2}\|\boldsymbol{x}\|_2^2, \tag{3}$$

where $\boldsymbol{A} \stackrel{\text{def}}{=} \boldsymbol{HP}$. Function f is quadratic and consequently has Lipschitz continuous gradient. The Lipschitz constant L_f is given by $\sigma_{max}^2(\boldsymbol{A})$, where $\sigma_{max}(\boldsymbol{A})$ is the maximum eigenvalue of operator $\boldsymbol{A}$. In practice, $\sigma_{max}(\boldsymbol{A})$ may be intractable to compute and, as we shall see, L_f need not be known at all to ACGM. However it is known that operator $\boldsymbol{A}$ is ill-conditioned and we can assume that function f has strong convexity parameter $\mu_f = 0$. Elastic net regularizer Ψ is not differentiable due to the l_1 term but has strong convexity parameter $\mu_\Psi = \lambda_2$. Hence, the objective as a whole has a strong convexity parameter of $\mu = \mu_\Psi = \lambda_2$.

ACGM does not require the exact form of the objective function. It instead relies on calls to its zeroth and first order operations, collectively referred to as "oracle functions" [22]. The splitting of the reconstruction problem in (3) yields four such oracle functions: $f(\boldsymbol{x})$, $\Psi(\boldsymbol{x})$, $\nabla f(\boldsymbol{x})$, and $\text{prox}_{\tau\Psi}(\boldsymbol{x})$, for $\boldsymbol{x} \in \mathbb{R}^n$ and $\tau > 0$. The gradient is given by

$$\nabla f(\boldsymbol{x}) = \boldsymbol{A}^T(\boldsymbol{Ax} - \boldsymbol{y}), \tag{4}$$

where $\boldsymbol{A}^T = \boldsymbol{P}^T\boldsymbol{H}^T$. The proximal operator, defined as

$$\text{prox}_{\tau\Psi}(\boldsymbol{x}) \stackrel{\text{def}}{=} \underset{\boldsymbol{z} \in \mathbb{R}^{m_t \times n_t}}{\arg\min} \left(\Psi(\boldsymbol{z}) + \frac{1}{2\tau}\|\boldsymbol{z} - \boldsymbol{x}\|_2^2 \right), \tag{5}$$

can be written in closed form (see also [19] and [23]) as

$$\text{prox}_{\tau\Psi}(\boldsymbol{x}) = \frac{1}{1 + \tau\lambda_2}\mathcal{T}_{\tau\lambda_1}(\boldsymbol{x}), \tag{6}$$

where the shrinkage operator $\mathcal{T}_\tau(\boldsymbol{x})$ is given by

$$\begin{gathered}(\mathcal{T}_\tau(\boldsymbol{x}))_{i,j} \stackrel{\text{def}}{=} (|\boldsymbol{x}_{i,j}| - \tau)_+ \operatorname{sgn}(\boldsymbol{x}_{i,j}), \\ \tau > 0, \quad i \in \{1, ..., m_t\}, \quad j \in \{1, ..., n_t\}.\end{gathered} \tag{7}$$

The structure of the objective function makes it possible to reduce the computational complexity of ACGM by departing from the oracle model. To estimate the local Lipschitz constant, operator $\boldsymbol{A}$ has to be applied at every iteration k to the new iterate $\boldsymbol{x}^{(k+1)}$. It is computationally inexpensive to cache these results by maintaining alongside the main iterate sequence $\boldsymbol{x}^{(k)}$, $k \in \{0, ..., k_{max}\}$ the sequence $\tilde{\boldsymbol{x}}^{(k)} = \boldsymbol{A}\tilde{\boldsymbol{x}}^{(k)}$. ACGM can be brought into an extrapolated form whereby an auxiliary point $\boldsymbol{z}^{(k+1)}$ can be obtained through linear extrapolation from $\boldsymbol{x}^{(k)}$ and $\boldsymbol{x}^{(k-1)}$. The new iterate $\boldsymbol{x}^{(k+1)}$ is computed based on the gradient of f at $\boldsymbol{z}^{(k+1)}$. The computational intensity of gradient expression (4) can be reduced as follows:

$$\nabla f(\boldsymbol{z}^{(k+1)}) = \boldsymbol{A}^T(\tilde{\boldsymbol{z}}^{(k+1)} - \boldsymbol{y}), \tag{8}$$

where

$$\tilde{\boldsymbol{z}}^{(k+1)} \stackrel{\text{def}}{=} \boldsymbol{A}\boldsymbol{z}^{(k+1)} = \tilde{\boldsymbol{x}}^{(k)} + \beta(\tilde{\boldsymbol{x}}^{(k)} - \tilde{\boldsymbol{x}}^{(k-1)}), \tag{9}$$

and β is the extrapolation factor.

The line-search stopping criterion [19] of ACGM at every iteration k is given by

$$\begin{aligned}f(\boldsymbol{x}^{(k+1)}) \leq f(\boldsymbol{z}^{(k+1)}) + \nabla f(\boldsymbol{z}^{(k+1)})^T(\boldsymbol{x}^{(k+1)} - \boldsymbol{z}^{(k+1)}) \\ + \frac{L^{(k+1)}}{2}\|\boldsymbol{x}^{(k+1)} - \boldsymbol{z}^{(k+1)}\|_2^2,\end{aligned} \tag{10}$$

where $L^{(k+1)}$ is the Lipschitz constant estimate at iteration k. Substituting gradient expression (4) and rearranging terms yields

$$\|\boldsymbol{A}(\boldsymbol{x}^{(k+1)} - \boldsymbol{z}^{(k+1)})\|_2^2 \leq L^{(k+1)}\|\boldsymbol{x}^{(k+1)} - \boldsymbol{z}^{(k+1)}\|_2^2. \tag{11}$$

We obtain a computationally efficient expression by reusing the precomputed values $\tilde{\boldsymbol{x}}^{(k+1)}$ and $\tilde{\boldsymbol{z}}^{(k+1)}$ as

$$\|\tilde{\boldsymbol{x}}^{(k+1)} - \tilde{\boldsymbol{z}}^{(k+1)}\|_2^2 \leq L^{(k+1)}\|\boldsymbol{x}^{(k+1)} - \boldsymbol{z}^{(k+1)}\|_2^2. \tag{12}$$

The global Lipschitz constant L_f can alternatively be expressed as

$$L_f = \sup_{\mathcal{D}_f} \frac{\|\boldsymbol{Ax}\|_2^2}{\|\boldsymbol{x}\|_2^2}. \tag{13}$$

In practice, the estimates are below this value and we set the initial one to

$$L^{(0)} = \frac{\|\boldsymbol{A}\boldsymbol{x}_0\|_2^2}{\|\boldsymbol{x}_0\|_2^2} = \frac{\|\tilde{\boldsymbol{x}}_0\|_2^2}{\|\boldsymbol{x}_0\|_2^2}. \tag{14}$$

Incorporating the above performance enhancements into ACGM in extrapolated form yields the method listed in Algorithm 1.

[2] A simpler version of ACGM was introduced in [21] to deal with the case of $\lambda_2 = 0$. The proposed method can be regarded as a computationally efficient generalization of this earlier scheme.

Algorithm 1 Proposed method

Input: $\boldsymbol{x}_0$, λ_1, λ_2, k_{max}
$\tilde{\boldsymbol{x}}^{(0)} := \boldsymbol{H}\boldsymbol{P}\boldsymbol{x}^{(0)}$
$\boldsymbol{x}^{(-1)} = \boldsymbol{x}^{(0)}$
$\tilde{\boldsymbol{x}}^{(-1)} = \tilde{\boldsymbol{x}}_0$
$L^{(0)} = \|\tilde{\boldsymbol{x}}^{(0)}\|_2^2 / \|\boldsymbol{x}^{(0)}\|_2^2$
$q^{(0)} = \frac{\lambda_2}{L^{(0)}+\lambda_2}$
$t^{(0)} = 0$
for $k = 0, ..., k_{max} - 1$ **do**
  $\alpha := 1 - q^{(k)}(t^{(k)})^2$
  $L^{(k+1)} := r_d L^{(k)}$
  loop
    $q^{(k+1)} := \frac{\lambda_2}{L^{(k+1)}+\lambda_2}$
    $t^{(k+1)} := \frac{1}{2}\left(\alpha + \sqrt{\alpha^2 + 4\frac{L^{(k+1)}+\lambda_2}{L^{(k)}+\lambda_2}(t^{(k)})^2}\right)$
    $\beta := \frac{t^{(k)}-1}{t^{(k+1)}} \frac{1-q^{(k+1)}t^{(k+1)}}{1-q^{(k+1)}}$
    $\boldsymbol{z}^{(k+1)} := \boldsymbol{x}^{(k)} + \beta(\boldsymbol{x}^{(k)} - \boldsymbol{x}^{(k-1)})$
    $\tilde{\boldsymbol{z}}^{(k+1)} := \tilde{\boldsymbol{x}}^{(k)} + \beta(\tilde{\boldsymbol{x}}^{(k)} - \tilde{\boldsymbol{x}}^{(k-1)})$
    $\tau := 1/L^{(k+1)}$
    $\boldsymbol{G} := \boldsymbol{P}^T\boldsymbol{H}^T(\tilde{\boldsymbol{z}}^{(k+1)} - \boldsymbol{y})$
    $\boldsymbol{x}^{(k+1)} := \frac{1}{1+\tau\lambda_2}\mathcal{T}_{\tau\lambda_1}(\boldsymbol{z}^{(k+1)} - \tau\boldsymbol{G})$
    $\tilde{\boldsymbol{x}}^{(k+1)} := \boldsymbol{H}\boldsymbol{P}\boldsymbol{x}^{(k+1)}$
    if $\|\tilde{\boldsymbol{x}}^{(k+1)} - \tilde{\boldsymbol{z}}^{(k+1)}\|_2^2 \leq L^{(k+1)}\|\boldsymbol{x}^{(k+1)} - \boldsymbol{z}^{(k+1)}\|_2^2$ **then**
      Break from loop
    else
      $L^{(k+1)} := r_u L^{(k+1)}$
    end if
  end loop
end for
Output: $\boldsymbol{x}^{(k_{max})}$

4. EXPERIMENTAL RESULTS

A three-step process was employed to simulate the RF ultrasound image: i) the calculation of the spatially-variant prototype PSFs; ii) the generation of the tissue reflectivity function (TRF); and iii) the spatially-variant convolution between the PSFs and the TRF, following the model described in (1) (Section 2).

The prototype PSFs were obtained in step i) using Field II, a realistic state-of-the art simulator [24, 25]. The simulation involved a linear 128-element ultrasound probe emitting ultrasound waves at a nominal frequency of 3 MHz. The width of each element was set to equal the wavelength (0.5 mm), while height was fixed at 5 mm. The distance between two consecutive elements was set to 0.1 mm. The transducer was excited using a two-period sinusoidal wave of frequency 3 MHz. The backscattered RF signals were sampled at a rate of 20 MHz. The prototype PSFs we obtained by placing isolated scatterers in front of the transducer with a distance in depth of 8.5 mm to each other. Ultrasound waves electronically focalized at 47 mm from the probe were emitted and the received echoes were statically focused prior to the delay-and-sum beamforming process. Hann apodization was used both for the emission and the reception.

The resulting $n_k = 10$ prototype PSFs are shown in Fig. 1. For the purpose of visualizing the areas influenced by individual prototype PSFs, they are displayed after envelope detection and min-max normalization centered at c_q for all $q \in \{1, ..., n_k\}$ in Fig. 1(a). To highlight the differences between individual prototype PSFs, they are displayed separately in Fig. 1(b). The 5th prototype PSF ($\boldsymbol{K}_5$) located at 43 mm from the probe was used in spatially-invariant deconvolution experiments. It is shown both in native form and after envelope detection in Fig. 2.

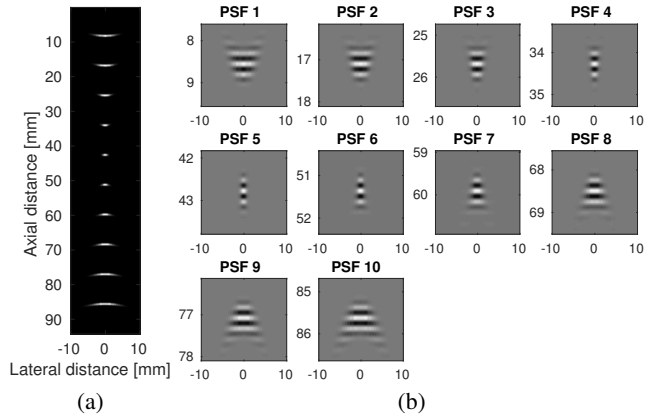

Fig. 1. Prototype PSFs generated with Field II for $n_k = 10$ depths at regularly spaced intervals of 8.5 mm. (a) Global view, after demodulation and min-max normalization, showing the location within the image of the prototype PSF centers; (b) Individual view, showing the spatial variance of the prototype PSFs.

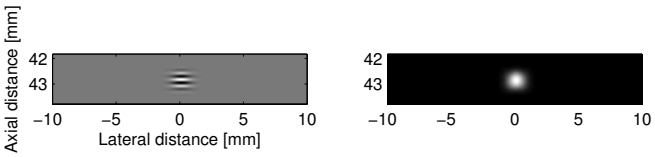

Fig. 2. The 5th prototype PSF $\boldsymbol{K}_5$ (left) and its demodulated version (right).

The TRF was obtained in step ii) following the classical procedure employed in ultrasound image simulation. A collection of uniform randomly located scatterers with zero-mean Gaussian random amplitudes has been generated. The standard deviation used to generate the amplitude of one scatterer depended on its location and was related, as suggested in the Field II simulator, to a digital image obtained from MRI and CT scans of a human kidney tissue. The number of scatterers was sufficiently large (10^5) to ensure fully developed speckle. The scatterer map was finally linearly interpolated onto a rectangular grid resulting into the TRF shown in Fig. 3(a).

In step iii), an ultrasound image was simulated from the TRF using the model in (1) to produce a starting point ($\boldsymbol{x}_0$) for the deconvolution experiments. First, the TRF was padded with a symmetric boundary. Next, the padded image was convolved with the spatially varying convolution operator $\boldsymbol{H}$, based on the prototype PSFs shown in Fig. 1. To simplify the hyperparameter tuning process, we have scaled $\boldsymbol{H}$ to ensure that $L^{(0)}$, as given by (14), is equal to 1. Finally, white Gaussian noise was added to the convolved image, such that the signal-to-noise ratio is 40 dB. The simulated ultrasound image is shown in B-mode representation in Fig. 3(b).

We have conducted two deconvolution experiments. Both used as starting point the simulated ultrasound image shown in Fig. 3(b) and the same values of the hyperparameters, $\lambda_1 = 0.005$ and $\lambda_2 = 0.01$, which were found by manual tuning to give the best results.

First, we have compared our method, which is able to integrate the spatial variability of the kernels in the deconvolution

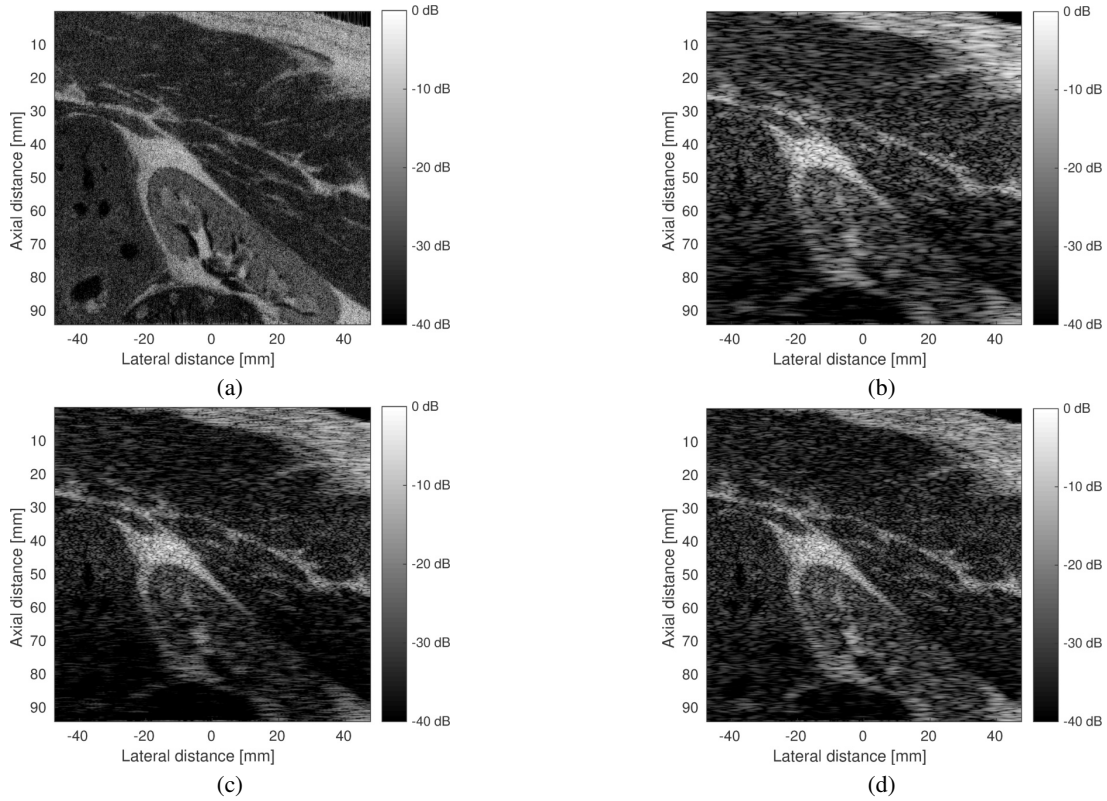

Fig. 3. (a) Ground truth of the tissue reflectivity function (TRF); (b) Observed B-mode image simulated from on the TRF in (a) using the image acquisition model in (1) employing the spatially-variant convolution operation based on the prototype PSFs in Fig. 1; (c) Spatially-invariant deconvolution result obtained using the fixed kernel $\boldsymbol{K}_5$ in Fig. 2; (d) Spatially-variant deconvolution result using our method.

process, with ACGM employing a spatially-invariant blur operator $\boldsymbol{H}$. Two restored images obtained after 150 iterations, are displayed in Fig. 3(c, d). The image in Fig. 3(c) was estimated considering a spatially-invariant PSF ($\boldsymbol{K}_5$ at 43 mm depth) and the one in Fig. 3(d) was obtained using our method. The quality of the deconvolution can be appreciated by comparing the restored images in Fig. 3(c, d) with the true TRF in Fig. 3(a). Note that the deconvolution results are also shown in B-mode. While the deconvolved images are similar in the vicinity of the focal point, our method manages to restore image features at the vertical extremities (Fig. 3(d)). These features are barely discernible both in the blurred image shown (Fig. 3(b)) as well as in the spatially-invariant PSF reconstruction (Fig. 3(c)). The simulation results support our previous claim that reconstruction quality of an image patch depends on the similarity between the blurring and the deblurring kernels applied to it, clearly demonstrating the superiority of our model.

The second experiment concerned optimization algorithms. We have compared the convergence behavior of our method to the state-of-the-art applicable to our model, in this case the Fast Iterative Shrinkage Thresholding Algorithm (FISTA) [26]. Fig. 4 shows the objective function values across iterations for the two methods. The convergence plot required an optimum value estimate $\hat{\boldsymbol{x}}^*$, which was obtained by running ACGM until floating point precision was exhausted. As predicted theoretically in [18, 19], the convergence rate of ACGM is linear. FISTA is unable to exploit the strong convexity of the objective and lags behind considerably.

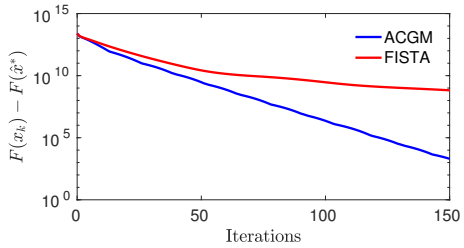

Fig. 4. Convergence rate of our method compared to FISTA.

5. CONCLUSION

We have devised a methodology for spatially-variant deconvolution of ultrasound images. Our method is theoretically guaranteed to converge linearly regardless of the structure of input data. In this respect, the reliability of our method is particularly of value to the stringent demands of the medical ultrasonography industry. Simulation results show that reconstruction is not only computationally tractable but has a rate that is competitive with existing approaches relying on far more restrictive assumptions. For that matter, our approach is able to address far more complex imaging models, even those that do not require horizontally-invariant PSF.

6. REFERENCES

[1] J. Ng, R. Prager, N. Kingsbury, G. Treece, and A. Gee, "Wavelet restoration of medical pulse-echo ultrasound images in an EM framework," *IEEE Trans. Ultrason. Ferroelectr. Freq. Control*, vol. 54, no. 3, pp. 550–568, 2007.

[2] R. Rangarajan, C. V. Krishnamurthy, and K. Balasubramaniam, "Ultrasonic imaging using a computed point spread function," *IEEE Trans. Ultrason. Ferroelectr. Freq. Control*, vol. 55, no. 2, pp. 451–464, Feb. 2008.

[3] H.-C. Shin, R. Prager, J. Ng, H. Gomersall, N. Kingsbury, G. Treece, and A. Gee, "Sensitivity to point-spread function parameters in medical ultrasound image deconvolution," *Ultrasonics*, vol. 49, no. 3, pp. 344 – 357, 2009.

[4] M. Alessandrini, S. Maggio, J. Poree, L. D. Marchi, N. Speciale, E. Franceschini, O. Bernard, and O. Basset, "A restoration framework for ultrasonic tissue characterization," *IEEE Trans. Ultrason. Ferroelectr. Freq. Control*, vol. 58, no. 11, pp. 2344–2360, 2011.

[5] C. Dalitz, R. Pohle-Frohlich, and T. Michalk, "Point spread functions and deconvolution of ultrasonic images," *IEEE Trans. Ultrason. Ferroelectr. Freq. Control*, vol. 62, no. 3, pp. 531–544, Mar. 2015.

[6] N. Zhao, A. Basarab, D. Kouamé, and J.-Y. Tourneret, "Joint segmentation and deconvolution of ultrasound images using a hierarchical Bayesian model based on generalized Gaussian priors," *IEEE Trans. Image Process.*, vol. 25, no. 8, pp. 3736–3750, 2016.

[7] O. Michailovich and D. Adam, "A novel approach to the 2-D blind deconvolution problem in medical ultrasound," *IEEE Trans. Med. Imag.*, vol. 24, pp. 86–104, Jan. 2005.

[8] O. Michailovich and A. Tannenbaum, "Blind deconvolution of medical ultrasound images: A parametric inverse filtering approach," *IEEE Trans. Image Process.*, vol. 16, no. 12, pp. 3005–3019, 2007.

[9] R. Jirik and T. Taxt, "Two dimensional blind Bayesian deconvolution of medical ultrasound images," *IEEE Trans. Ultrason. Ferroelectr. Freq. Control*, vol. 55, no. 10, pp. 2140–2153, 2008.

[10] C. Yu, C. Zhang, and L. Xie, "A blind deconvolution approach to ultrasound imaging," *IEEE Trans. Ultrason. Ferroelectr. Freq. Control*, vol. 59, no. 2, pp. 271–280, 2012.

[11] J. G. Nagy and D. P. O'Leary, "Restoring images degraded by spatially variant blur," *SIAM J. Sci. Comput.*, vol. 19, no. 4, pp. 1063–1082, 1998.

[12] O. V. Michailovich, "Non-stationary blind deconvolution of medical ultrasound scans," in *Proc. SPIE*, Mar. 2017, vol. 101391C.

[13] L. Roquette, M. M. J.-A. Simeoni, P. Hurley, and A. G. J. Besson, "On an Analytical, Spatially-Varying, Point-Spread-Function," in *Proc. IEEE Ultrason. Symp. (US)*, 2017.

[14] H. Zou and T. Hastie, "Regularization and variable selection via the elastic net," *J. Roy. Stat. Soc. Ser. B*, vol. 67, no. 2, pp. 301–320, 2005.

[15] C. Quinsac, A. Basarab, and D. Kouamé, "Frequency domain compressive sampling for ultrasound imaging," *Advances in Acoustics and Vibration*, vol. 12, pp. 1–16, 2012.

[16] T. Szasz, A. Basarab, M.-F. Vaida, and D. Kouamé, "Elastic-net based beamforming in medical ultrasound imaging (regular paper)," in *Proc. IEEE Int. Symp. Biomed. Imaging (ISBI)*, Apr. 2016, Prague, Czech Republic, pp. 477–480.

[17] B. Byram, "Aperture domain model image reconstruction (admire) for improved ultrasound imaging," in *Proc. IEEE Int. Conf. Acoust., Speech, and Signal Processing (ICASSP)*, Mar. 2017, pp. 6250–6253.

[18] M. I. Florea and S. A. Vorobyov, "An accelerated composite gradient method for large-scale composite objective problems," *arXiv preprint arXiv:1612.02352*, Dec. 2016.

[19] M. I. Florea and S. A. Vorobyov, "A generalized accelerated composite gradient method: Uniting Nesterov's Fast Gradient Method and FISTA," *arXiv preprint arXiv:1705.10266*, May 2017.

[20] M. I. Florea, A. Basarab, D. Kouamé, and S. A. Vorobyov, "An axially-variant kernel imaging model for ultrasound image reconstruction," *arXiv preprint arXiv:1801.08479*, Jan. 2018.

[21] M. I. Florea and S. A. Vorobyov, "A robust FISTA-like algorithm," in *Proc. IEEE Int. Conf. Acoust., Speech, and Signal Processing (ICASSP)*, Mar. 2017, New Orleans, USA, pp. 4521–4525.

[22] A. Nemirovski, D. B. Yudin, and E. R. Dawson, *Problem complexity and method efficiency in optimization*, John Wiley & Sons, Inc., Hoboken, NJ, USA, 1983.

[23] N. Parikh, S. P. Boyd, et al., "Proximal algorithms," *Foundations and Trends in optimization*, vol. 1, no. 3, pp. 127–239, 2014.

[24] J. A. Jensen and N. B. Svendsen, "Calculation of pressure fields from arbitrarily shaped, apodized, and excited ultrasound transducers," *IEEE Trans. Ultrason. Ferroelectr. Freq. Control*, vol. 39, no. 2, pp. 262–267, Mar. 1992.

[25] J. A. Jensen, "Field: A program for simulating ultrasound systems," *Med. Biol. Eng. Comput.*, vol. 34, pp. 351–353, 1996.

[26] A. Beck and M. Teboulle, "A fast iterative shrinkage-thresholding algorithm for linear inverse problems," *SIAM J. Imag. Sci.*, vol. 2, no. 1, pp. 183–202, 2009.